Variability of the kinetic energy in seasonally ice-covered oceans.

Josué Martínez-Moreno[1], Camille Lique[1], Claude Talandier[1], Quentin Jamet[2], Anne-Marie Treguier[1]

[1]Laboratoire d'Océanographie Physique et Spatiale (LOPS), University of Brest/IFREMER/IRD/CNRS, Brest, France
[2]Service hydrographique et océanographique de la marine (SHOM), Brest, France

Key Points:

- Seasonal variations in Arctic sea ice significantly influence the ocean's scales of motion.
- Between summer and winter, the dominant scales of motion in the Arctic transition from mesoscale to submesoscale.
- Sea ice dissipates preferentially the mesoscale range of motion in winter, and the inverse energy cascade enhances the mesoscale in summer.

Corresponding author: Josué Martínez-Moreno, `josue.martinez.moreno@ifremer.fr`

Abstract

The seasonality of Arctic sea ice cover significantly influences heat, salt, buoyancy fluxes, ocean-ice stresses, and the potential and kinetic energy stored in the ocean mixed layer. This study examines the seasonal variability of oceanic scales and cross-scale flux of kinetic energy in the seasonally ice-covered Arctic, using a high-resolution, idealized coupled ocean-sea ice model. Our simulations demonstrate pronounced seasonality in the scales of oceanic motion within the mixed layer, governed by distinct mechanisms during summer and winter. In summer, an inverse energy cascade sustains mesoscale dynamics and enhances kinetic energy. In winter, ice-induced dissipation suppresses kinetic energy and mesoscale, allowing only the persistence of submesoscale features. These results underscore the critical role of sea ice in modulating the seasonal dynamics of oceanic motion and their dominant scales, a behavior markedly different from that in the open ocean. Thus, understanding these coupled processes is essential for improving predictions of the ocean's energy evolution as the Arctic transitions toward a summer ice-free regime.

Plain Language Summary

The seasonal changes in Arctic ice cover significantly influence heat, salt, and energy transfers within the ocean. This study employs a high-resolution model to investigate how these variations affect the seasonality of ocean currents and energy distribution throughout the year. Our findings reveal that the scale of ocean motion and the amount of kinetic energy differ between summer and winter. In summer, ocean scales exceed 8 km and exhibit higher energy levels. Conversely, in winter, sea ice dissipates oceanic energy, reducing energy levels, and limiting motion to scales smaller than 8 km. These results demonstrate that sea ice plays a pivotal role in shaping the seasonal dynamics of oceanic processes, a behavior that contrasts with the open ocean. Understanding these seasonal changes is critical for predicting how the Arctic will evolve as it transitions toward a summer ice-free state.

1 Introduction

Oceanic eddies are ubiquitous in the Arctic Ocean, particularly in seasonally ice-covered regions (Cassianides et al., 2023). Arctic eddies are known to stir and mix ocean properties (Fine et al., 2018), modulate the ocean stratification (Pnyushkov et al., 2018), contribute to the equilibration of the large scale wind-driven circulation (Lique & Johnson, 2015), transport nutrients and tracers (Watanabe et al., 2014), and transfer ocean heat vertically (Bebieva & Timmermans, 2016). Eddies with horizontal length-scales of the same order as the first baroclinic Rossby deformation radius ($O \sim 10\ km$; Nurser & Bacon, 2014) are known in literature as mesoscale, while smaller scales are commonly referred to as submesoscale. Mesoscale eddies generated through baroclinic instabilities and submesoscale eddies generated by mixed layer instabilities and shear/strain of mesoscale eddies are known to transfer potential energy into kinetic energy (KE; Fox-Kemper et al. 2008. Moreover, mesoscale and submesoscale eddies are capable to transfer KE across scales from large scales toward smaller scales (the forward energy cascade) and from small to larger scales (the inverse energy cascade; Ferrari & Wunsch 2009). An improved understanding of the seasonality of KE and flow scales in the open ocean has been gained over the past decade (Rocha et al., 2016; Buckingham et al., 2016; Qiu et al., 2014). In a nutshell, in the open ocean, the seasonality is characterized by more energy within the mesoscale range and a drop of energy within the submesoscale range in summer, while, in winter the energy in the mesoscale retains its summer signature, but the energy in the submesoscale range increases due to a deepening of the mixed layer (ML) and an enhancement of ML instabilities (Yu et al., 2023; Uchida et al., 2017). In the ice-covered ocean, the seasonality of the ocean dynamics, stratification, and ML are strongly dominated by the growth, melt, and surface stress of the sea ice, thus we hypothesize that the seasonality of KE spectra could differ from the open ocean regime.

Several studies have explored the seasonal dynamics of submesoscale and mesoscale flows in polar regions, particularly under varying sea ice conditions. Using an idealized model representing the multi-year sea ice pack, Mensa & Timmermans (2017) showed that submesoscale KE increases during summer due to enhanced internal wave activity, whilst the mesoscale KE shows no seasonal variation, both in the ML and the ocean interior. In contrast, based on the analysis of realistic high-resolution simulations, Manucharyan & Thompson (2022) and Liu et al. (2024) found a seasonal variability of the KE and the oceanic scales of motion in the seasonally ice-covered regions. In particular, Manucharyan & Thompson (2022) noted a seasonal transition from an energetic mesoscale and weak submesoscale field in summer to a weak mesoscale and energetic submesoscale field in winter (see Fig. 3g in Manucharyan & Thompson 2022), likely associated with the transition from high sea ice concentrations in winter to lower concentrations in summer. Additionally, they found that the vorticity variance was more strongly dissipated in winter than in summer due to the higher sea ice concentration. Although the findings of these studies might initially seem opposed, one need to remember that they consider different sea ice regimes: Mensa & Timmermans (2017) focused on the ice pack, while the other two studies focused on the seasonal ice-covered zones and qualitatively described a dependency between the energetic ocean scales and the sea ice concentration. However, the seasonal transition of ocean scales and their energetics under sea ice, as the ocean shifts seasonally from ice-free to ice-covered conditions, remains to be fully characterized.

Determination from direct observations of the predominant ocean scales of motion seasonality in the Arctic is limited, but recent observational studies have provided some evidence supporting a seasonality of the mesoscale field. For instance, Meneghello et al. (2021) suggested using moorings and numerical simulations that the growth of surface mesoscale eddies in summer is modulated by sea ice friction, and Cassianides et al. (2023) found hints of a seasonal variability of the slopes of the surface potential density spectra from Ice Tethered Profilers in the seasonally ice-covered Canadian and Eurasian basins. Potential density variance is directly linked to baroclinic instability due to the conservation of potential vorticity. Thus, seasonal variations of the scales in the potential density variance are likely evidence of a seasonal variation of the ocean scales of motion under sea ice. Yet, it remains unclear which processes may be driving this seasonality. Here, we focus on the drivers of the seasonality of scales and KE as the ocean transitions from ice-free to ice-covered conditions over a full seasonal cycle.

Sea ice dissipates ocean eddies (Ou & Gordon, 1986), through friction and a process equivalent to the 'eddy-killing' used in ocean-atmosphere interactions (Renault et al., 2016), where wind stress dissipates the oceanic eddies. Indeed, ice stress can act similarly by diminishing the intensity of the ocean eddy field. As sea ice drifts, it exerts stress on the ocean surface, and if the ice stress opposes the eddies' circulation, eddies will lose energy due to friction with the ice. Thus the intensity and coherence of the eddies will be reduced asymmetrically, thereby 'killing' or weakening them, similar to how wind stress weakens eddies in ice-free regions. This interaction is the largest in seasonal ice-covered regions, where the mobility of the ice varies throughout the year. It is well known that 'eddy killing' acts preferentially at given length-scales (Rai et al., 2021), thus we hypothesize that this ice-induced eddy dissipation may also act preferentially within a range of oceanic scales, and vary on a seasonal cycle with the varying sea ice conditions. This framework has been commonly used in ocean-atmosphere interactions, and here, for the first time, we apply it to ocean-ice interactions.

This paper is structured as follows: Section 2 details the methodology employed in our study. Section 3.1 examines the seasonal transition of scales within the idealized simulation. In Section 3.2, we analyze the KE spectra, the generation of mesoscale and submesoscale eddies, and the seasonality of the forward and inverse energy cascade. Sec-

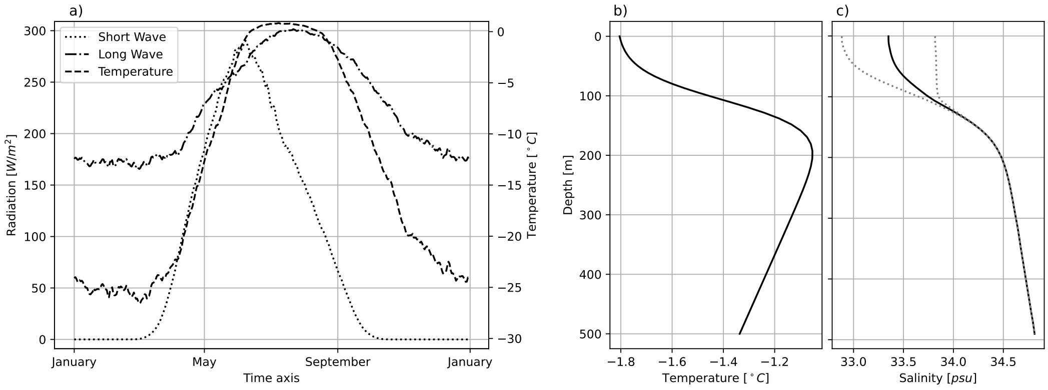

Figure 1. Forcing and vertical initial profiles of the idealized configuration. (a) Incoming short wave radiation, incoming long wave radiation, and air temperature. Vertical profiles of (b) temperature and (c) salinity for the initial conditions of the simulation. In panel c, the dotted lines correspond to the northern and southern vertical salinity profiles of the simulation. Note that the temperature profile was adjusted to match the freezing point at the surface based on the mean salinity profile.

tion 3.3 explores the sources and sinks of KE of the simulation. Finally, Section 4 presents our discussion and conclusions, synthesizing the findings and their implications for the dynamics of the Arctic Ocean.

2 Methods

2.1 Model configuration

We use an hydrostatic ocean model (NEMO; Madec et al., 2022) coupled to an elasto-viscoplastic sea ice model (SI3; NEMO Sea Ice Working Group, 2022). The setup used for the idealized configuration consists of a zonally reentrant channel that spans 300 km meridionally, 200 km zonally, and 500 m in depth. The horizontal resolution is 250 m and the vertical has 50 levels with variable spacing that increases from 2.5 m at the surface to 19 m at the bottom. This resolution was chosen to resolve mesoscale and submesoscale features arising from baroclinic instabilities prescribed in the initial conditions. We opted for a logarithmic bottom drag to reduce flow length-scales, but note that the KE seasonality remains consistent when using a free-slip bottom, though both the flow intensity and scales are smaller. We use an f-plane approximation at 80° N ($f = 1.43\times 10^{-4}$), a velocity dependent bi-harmonic isopycnal tracer diffusivity, and a bi-harmonic horizontal viscosity. The vertical mixing is based on the turbulent kinetic energy closure from Blanke & Delécluse (1993). We use the Non-Penetrative Convective algorithm parameterization that mixes iteratively the water column until the density profile is stable. A nonlinear equation of state is used to compute density (EOS80; Fofonoff & Millard Jr 1983). The atmospheric forcing consists of a daily climatology of shortwave radiation, longwave radiation, and air temperature built from ERA5 over the period 1979 to 2021 over the Arctic (north of 80°N; Fig. 1a). This forcing is spatially constant, and it does not include wind forcing. The seasonal cycle of the forcing allows the retreat and formation of sea ice during summer and winter, respectively. The surface fluxes between the ice-ocean-atmosphere are computed using the NCAR bulk formula (Large & Yeager, 2009).

The simulation is a spin-down experiment initialized with a meridional front prescribed only in the salinity field (Fig. 2a and b), since the density in the Arctic is mostly controlled by salinity. The front is generated by redistributing meridionally a $\sim 1\ psu$ salinity anomaly that extends down to 75 m depth, with a fresh anomaly in the northern half of the domain (Fig. 1c). The temperature and salinity fields include noise in the top 75 m to seed baroclinic instability. Our simulation is initialized from rest on May 1st with a sea ice thickness of 1 m over the entire model domain and it spins down over time. The background initial vertical temperature and salinity profiles resemble the vertical structure of the Arctic with fresh and cold water masses above warmer and saltier waters below the halocline (Fig. 1b and c). Baroclinic instabilities develop around the initial front and it takes a seasonal cycle for the ML, stratification, and sea ice to equilibrate. This seasonality of the simulation was tested and consistent across multiple horizontal resolutions: $2km$, $250m$, and $100m$. The analysis presented hereafter uses daily output during the second year of the $250m$ resolution simulation. The simulation reproduces the seasonality of the ice cover, with the sea ice extent maxima occurring in May (before the forcing maxima of incoming short wave radiation; Fig. 1a), and the domain is ice-free between August and October.

2.2 Energetics framework

The KE budget and potential energy budget equations share the term wb, where w is the vertical component of the velocities and b the buoyancy, i.e. the buoyancy flux, that represents the conversion from potential energy to KE and vice-versa. A decomposition of this term, allows us to decompose it into the conversions of mean potential energy to mean kinetic energy and eddy potential energy (EPE) to eddy kinetic energy (EKE):

$$wb = \overline{w}\overline{b} + w'b' + \mathcal{O}. \tag{1}$$

In our simulation, the geometry ensures that the average along the periodic direction, $\overline{}$, represents the mean state of the domain, with deviations from this mean, denoted as $'$. Averaging and rearranging the equation, the cross terms ($\mathcal{O}$) become zero and we obtain:

$$\overline{w'b'} = \overline{wb} - \overline{w}\overline{b}. \tag{2}$$

This term is commonly known as the baroclinic conversion rate, turbulent potential to EKE conversion rate, or eddy buoyancy flux (Wunsch & Ferrari, 2004).

The ocean contains energy on a wide range of length-scales and frequencies. To understand the scales in which energy is contained, we use the spectral energy flux (Π_Q) defined by Capet et al. (2008). The momentum equation are Fourier transformed to obtain the KE budget equation in wavenumber domain:

$$\frac{\partial}{\partial t} KE(k_x, k_y, t) = T(k_x, k_y, t) + P(k_x, k_y, t) - D(k_x, k_y, t). \tag{3}$$

Here, k_x and k_y are the wavenumbers in the x and y direction, $P(k_x, k_y, t)$ is the forcing term including the conversion rate from potential energy to KE, $D(k_x, k_y, t)$ the dissipation, and $T(k_x, k_y, t)$ emerges from the advection term of the momentum equation and corresponds to the transfer of KE among different spatial scales:

$$T(k_x, k_y, t) = \Re\left[\mathcal{F}(u)^*\mathcal{F}\left(u\frac{\partial u}{\partial x} + v\frac{\partial u}{\partial y}\right) + \mathcal{F}(v)^*\mathcal{F}\left(u\frac{\partial v}{\partial x} + v\frac{\partial v}{\partial y}\right)\right]/\Delta k^2, \tag{4}$$

where $\Re$ means the real part of the expression and $\mathcal{F}$ the Fourier Transform. Finally, the spectral KE flux Π_Q is obtained by integrating $T(k_x, k_y, t)$ from wavenumber K' to the maximum available wavenumber (K; $\sim 2cpkm$).

$$\Pi_Q(K', t) = \sum_{K > K'} T(k_x, k_y, t). \tag{5}$$

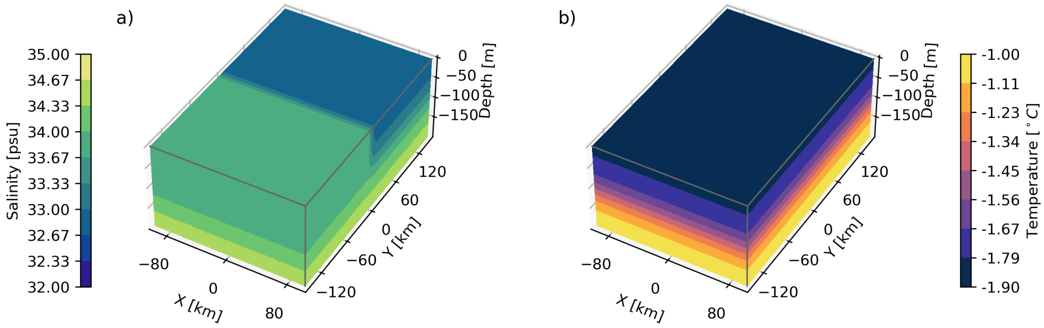

Figure 2. Initial conditions for the idealized coupled sea ice-ocean configuration. a) Initial ocean salinity initialized with a fresher northern domain within the ML to develop baroclinic instabilities. The salinity difference between the northern and southern half of the domain is 1 psu. b) Initial ocean temperature representative of waters near the freezing point above a warmer subsurface layer.

The spectral KE flux and KE spectra are computed for all the meridional transects (along the periodic size of the domain) between $-125km$ and $125km$ to avoid the effect of the northern and southern boundaries and then averaged meridionally. The KE spectra is computed for snapshots on the 1st December, 1st March, 1st June, and 1st of September, with a spread that corresponds to the maximum and minimum values of the meridional spectra. The spectral KE flux is averaged over each season and it represents the mean transfer of energy from the start of one season to the start of the following one. For example, the summer energy flux corresponds to the mean energy transfer contributed to transition from the energy distribution on the 1st of June to that on the 1st of September.

2.3 Mixed layer instabilities

Frontal structures within the ML can result in the generation of a submesoscale eddy field through ageostrophic baroclinic instabilities (Fox-Kemper et al., 2008). These instabilities extract potential energy by flattening isopycnals and inject KE into a ML eddy field. The generation of submesoscale eddies intensifies in regions with strong lateral buoyancy gradients, high vorticity, and weak vertical stratification, which can be quantified using the balanced Richardson number

$$Ri = \frac{N^2 f^2}{M^4}, \tag{6}$$

where f is Coriolis and N^2 is the vertical stratification defined as

$$N^2 = -\frac{g}{\rho_0}\frac{\partial \rho}{\partial z}, \tag{7}$$

g is the gravity, ρ_0 is the average ocean density of $1026kg/m^3$, and ρ is the density. M^4 is the square of the horizontal buoyancy gradients,

$$M^4 = \frac{\partial b}{\partial x} + \frac{\partial b}{\partial y}. \tag{8}$$

By introducing the Richardson angle (ϕ_{Ri}), the instability regimes can be classified into stable conditions, symmetric instabilities, and gravitational instabilities (Thomas et al., 2013):

$$\phi_{Ri} = tan^{-1}\left(-\frac{1}{Ri}\right), \tag{9}$$

instabilities will occur if the following criteria is meet:

$$\phi_{Ri} < \phi_c \equiv tan^{-1}\left(-\frac{\zeta_g}{f}\right) \tag{10}$$

where ζ_g is the vertical component of the absolute vorticity of the geostrophic flow. Due to the hydrostatic approximation in NEMO, the ocean model can only represent ageostrophic baroclinic symmetric instabilities ($N^2 > 0$), as any density inversion is mixed by the non-penetrative convection parameterization. The contribution of each of these instabilities to the KE budget are quantified by the baroclinic conversion term (Eq. 1; Thomas et al. 2013). The characteristics of ML instabilities can be captured using the Eady theory (Eady, 1949), which was extended by Stone (1972) to include ageostrophic baroclinic instabilities. The spatial scale of the fastest growing mode is defined as:

$$L_s = \frac{2\pi U}{|f|}\sqrt{\frac{1+Ri}{5/2}}, \tag{11}$$

where U is the mean flow velocity, and the Eady time-scale is defined as:

$$T_s = \sqrt{\frac{54}{5}}\frac{\sqrt{1+Ri}}{|f|}, \tag{12}$$

Fox-Kemper et al. (2008) suggest that the Eady growth rate is a good estimate of the growth length-scale only during the spin up of the instabilities, yet, this linear theory is helpful in determining the presence and persistence of ML instabilities in the numerical simulations.

2.4 Eddy dissipation by sea ice

The stress at the ocean surface ($\boldsymbol{\tau}_o$) is estimated by adding the quadratic form stress drag from the atmosphere and the ice as follows:

$$\boldsymbol{\tau}_o = (1-A)\boldsymbol{\tau}_a + A\boldsymbol{\tau}_i, \tag{13}$$

where A is the ice concentration, τ_a the atmosphere stress, and τ_i the ice stress. As the winds are set to zero in our simulation, we obtain:

$$\boldsymbol{\tau}_o \approx A\boldsymbol{\tau}_i. \tag{14}$$

And the stress exerted by the sea ice is equal to:

$$\boldsymbol{\tau}_i = \rho_0 C_D|\mathbf{u}_i - \mathbf{u}_o|\left(\mathbf{u}_i - \mathbf{u}_o\right). \tag{15}$$

Here, C_D the drag coefficient of $12{\times}10^{-3}$, $\mathbf{u}_i$ the ice velocity, and $\mathbf{u}_o$ the surface ocean velocities. Analogous to the wind work and eddy killing proposed by Renault et al. (2016), we define the ice work or ice-induced eddy dissipation (FK) as:

$$FK = \frac{1}{\rho_0}\left(\overline{\tau_{i_x} u_i} + \overline{\tau_{i_y} v_i}\right) \tag{16}$$

where u_i and v_i are the zonal and meridional ice velocities, τ_{i_x} and τ_{i_y} are the zonal and meridional surface ice stresses. This ice work can act to dissipate the energy contained by the eddy field, and using spectral analysis of the ice work, we can estimate the scales at which the eddy field is dissipated by the sea ice stress.

3 Results

3.1 Seasonality of the ice-ocean conditions

The seasonality of the atmospheric forcing (air temperature, incoming shortwave, and longwave radiation; Fig. 1a) are reflected in the seasonality of the domain averaged sea ice thickness, and temperature and salinity profiles (Fig. 3a and b). The sea ice thickness (overlaid to Fig. 3a) shows a characteristic seasonal cycle ranging from $0m$ in summer to $\sim 2m$ thickness in May. During summer, sea ice melt releases freshwater at the ice-ocean interface, forming a shallow summer ML. Additionally, a surface warm layer forms and becomes trapped below the ML, forming a remanent layer that persists until the next winter between the ML and the halocline. The trapped heat in this remanent layer is known to modulate the growth of sea ice in the following season as the ML deepens and this warm layer is entrained into the ML (Cole et al., 2010; Mensa & Timmermans, 2017). In winter, sea ice growth rejects brine, deepening the ML to around $90m$ depth, slightly deeper than basin averaged ML depths observed in the Arctic ($\sim 60m$; Zhai & Li 2023). The ML temperature in winter remains near the freezing point (a function of salinity and pressure; Fofonoff & Millard Jr 1983). In May, at the start of the melting season, the ML initially shoals, then briefly deepens, before eventually stabilizing at a shallower depth. This occurs because the ocean surface freshens and the freezing point raises, allowing sea ice to briefly regrow, which causes brine rejection and a sudden deepening of the ML. As surface warming continues in response to the atmospheric forcing, the ML equilibrates and reaches a depth of $\sim 10m$ in summer. The vertical stratification, also presents a seasonal cycle consistent with observations (Fig. 3c; Cole & Roemer 2024). During winter, the surface layer thickens due to brine rejection and mixing, which weakens the vertical stratification. In contrast, in summer, the input of warm and fresh water at the surface increases buoyancy and strengthens the vertical stratification between the surface and the ocean interior.

The pattern seen in the vertical stratification is similar to that of the horizontal buoyancy gradients (M^2; Fig. 3d), albeit with a weaker horizontal buoyancy gradients at the surface during the ice-free months (August-October). During the ice-covered period (winter and spring), a large horizontal buoyancy gradient is found near the ML depth, likely linked to ML instabilities and the presence of submesoscale processes (Timmermans et al., 2012; Thomas et al., 2013). KE reveals a more energetic ocean in summer, starting when the ice starts to melt (June) and ending when ice re-growths in October (Fig. 3e). During the same period, the surface layer associated with high KE thickens from $\sim$ 100 m depth to up to $\sim$ 150 m depth. These summer changes are likely consequence of the absence of sea ice, which reduces dissipation of ocean currents and facilitates the generation of eddies in the halocline(Zhao et al., 2014). During the rest of the year, KE is at least one order of magnitude smaller and is generally constrained to the top $\sim$ 100 m depth. Note that the Hovmöller diagrams exhibit a seasonality that is not entirely periodic due to the spin-down nature of the simulation, despite this, the modeled seasonal cycle remains consistent during the subsequent years of the simulation (not shown).

The seasonality of KE is further explored by comparing time series of the ocean velocity magnitude ($|\vec{u}_o|$) and ice velocity magnitude ($|\vec{u}_i|$; Fig. 4b). On average, the ocean velocity is approximately $0.02m/s$, and it peaks during the ice-free months (Fig. 4a). The ice velocity is on average $\sim 0.003m/s$ and it exhibits two prominent peaks: one in July, during ice melt, and another in October, during ice refreezing (Fig. 4a). During these two periods and because our simulations exclude wind forcing, the velocities of ice and ocean are highly correlated, with a correlation coefficient of ~ 0.7 (Fig. 4b), indicating that the ice is moving at the same speed and scales as the ocean, thus resulting in minimal stresses between the ice and the ocean (Eq. 15). In contrast, during winter and spring, the ice-ocean velocity correlation weakens, leading to increased stress as the motion of ice and ocean differentiate. Further evidence of this is shown in the seasonally averaged

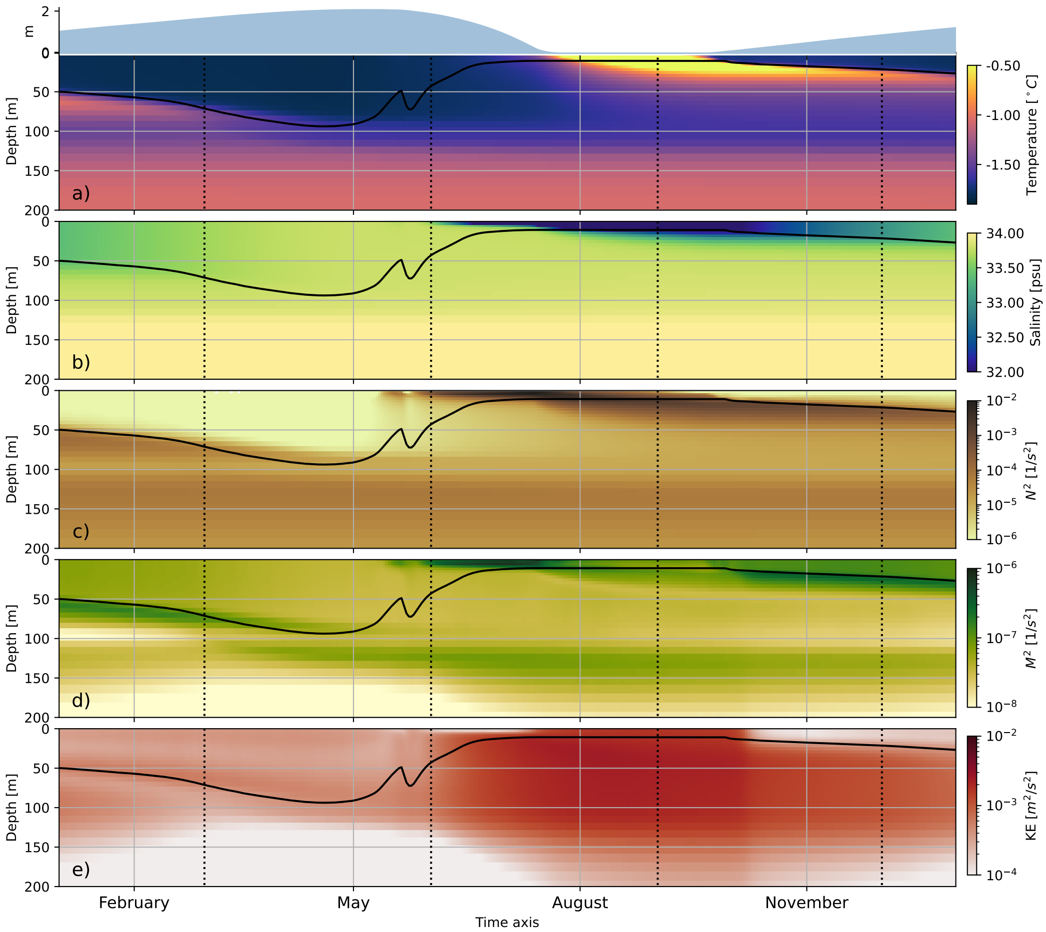

Figure 3. Hovmöller diagrams during the second year of the simulation show the domain averaged (a) temperature, (b) salinity, (c) mean Brunt-Väisälä frequency (N^2; vertical stratification), (d) mean horizontal buoyancy gradients (M^2), and e) mean kinetic energy. Additionally, the mixed layer depth is shown with the black solid line in all panels. The ice volume is shown above panel a). Vertical dotted lines correspond to the first day of the different seasons.

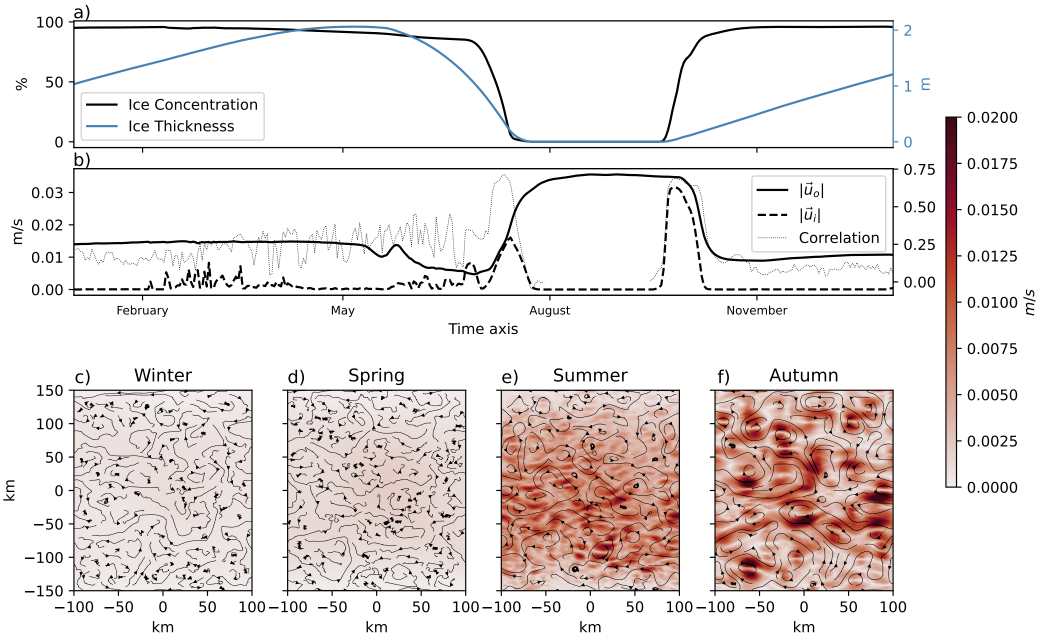

Figure 4. Time-series of the domain average (a) ice concentration and thickness, and (b) ocean surface velocity magnitude ($|\vec{u}_o|$) and ice velocity magnitude ($|\vec{u}_i|$). The dotted line corresponds to the Spearman correlation coefficient between the ocean and ice velocities for each day of the second year of the simulation. Seasonally averaged ice velocity magnitude and streamlines are shown for c) winter, d) spring, e) summer, and f) autumn.

ice velocity magnitudes (Fig. 4c-f). In winter and spring (Fig. 4c and d), the ice velocity magnitude is nearly uniform, with a large-scale but very small speed across the simulation domain. Conversely, in summer and autumn (Fig. 4e and f), the ice velocity patterns show greater variability and the ice velocity scales match closely those of the ocean. The transition from ice-covered to ice-free conditions and vice-versa results in a seasonal variability of the ocean and ice velocities, which in turn modulate the ocean surface stress and the KE budget.

Figure 5 shows summer and winter snapshots of the KE and normalized vorticity. In the winter snapshot (1st of March, Fig. 5a and c), the field is highly heterogeneous with scales smaller than the Rossby radius of deformation ($R_D \sim 8\ km$ over the year). The mean KE over the first 100m is $\sim 1.6{\times}10^{-4}\ m^2/s^2$ and the dominant spatial scale is in the order of a few kilometers. This spatial scale in addition to the large normalized vorticity values (Fig. 5c) suggest the presence of submesoscale dynamics during winter. In contrast, in summer (1st of September, Fig. 5b and d) the domain is ice-free and the scale of the flow become larger than 10 km (i.e. larger than the R_D). The mean KE over the first 100m is $\sim 1{\times}10^{-3}\ m^2/s^2$, one order of magnitude larger than the KE in the winter snapshot, consistent with Figure 3b. This larger spatial scale in addition to an increase in KE and smaller normalized vorticity values (Fig. 5d) suggest the presence of mesoscale dynamics in summer. Overall, the deformation radius and the seasonal variability of the normalized vorticity corroborate the seasonality of the dominant flow scales from submesoscale in winter to mesoscale in summer. The subsequent sections elaborate on the potential drivers of KE seasonality, including the transfer of KE among the different spatial scales ($T(k_x, k_y, t)$), the conversion of EPE to EKE ($w'b'$), and the dissipation by sea ice.

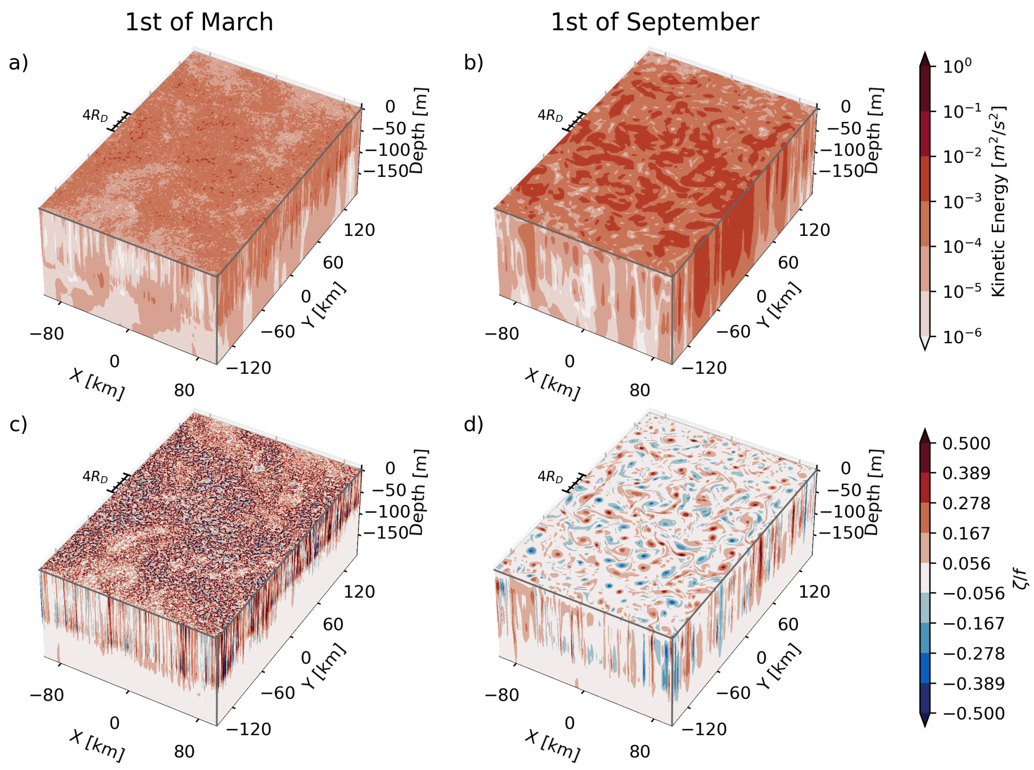

Figure 5. Snapshot on KE (top; panels a and b) and normalized vorticity (ζ/f) (bottom; panels c and d) on the 1st of March (left column) and the 1st of September (right column). A scale of four times the Rossby radius is shown in all panels ($4R_D$).

3.2 Seasonality of the kinetic energy cascade

The KE spectra and spectral KE flux are calculated to quantify the scale seasonality and energy transfers between scales. The KE spectra for a snapshot at the beginning of each season are shown in Figure 6. Near the surface, at 20m depth (Fig. 6a), the KE spectra reveals a pronounced variability of the KE contained within each length-scale, particularly within the mesoscale range. This variability is exemplified by contrasting the spectra in ice free conditions (1st of September) and ice covered conditions (1st of March). During ice free months, the KE spectra exhibits more energy within the mesoscale range. This suggests a prevalence of eddies with a Rossby radius greater than $8km$ (R_D). In contrast, the spectra for the ice covered conditions reveal a decrease in the energy at mesoscale and a gain of energy at submesoscale, indicative of an intensified smaller-scale field ($< R_D$). The 1st of December and 1st of June spectra resemble that of the 1st of March, because at these dates, the domain is fully ice-covered. Looking at the periods in which ice melts and forms, the spectra transitions between these two states. Evidence of this is shown in the monthly averaged spectra in the supplementary Figure **??**. These variations are consistent with the seasonality of KE in high-resolution realistic simulations (see Fig. 3g of Manucharyan & Thompson 2022). At 150m depth, where the ocean environment is less influenced by surface fluxes and the ice cover (Fig. 3b), the KE spectra is less energetic. Furthermore, at this depth there is a difference between the 1st of September and 1st of December, and the 1st of March and 1st of June likely due to the generation of eddies within the halocline.

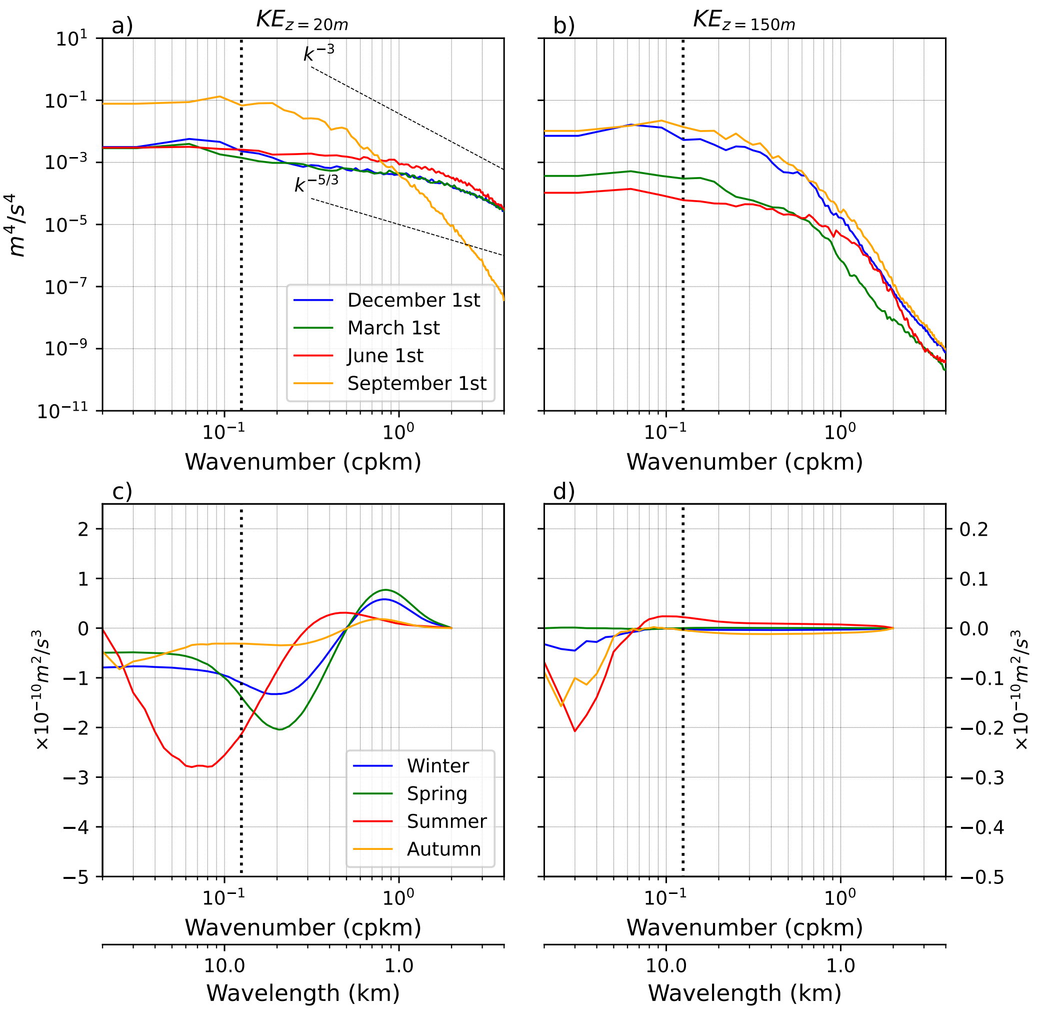

Figure 6. Kinetic energy spectra snapshots a) at 20m depth and b) at 150m depth for the first day of each season (1st December, 1st March, 1st June, and 1st of September). Kinetic energy flux averaged for each season at c) 20m and d) 150m depth. Vertical dotted line correspond to the Rossby radius (R_d). The dashed lines correspond to the -3 and $-5/3$ slopes typical of KE spectra. The shaded areas show the spread of the spectral energy across the meridional direction of the simulation.

According to 2D turbulence (Charney, 1971; Vallis, 2017), the open-ocean power laws (kinetic energy spectral slopes) are approximately k^{-3} and $k^{-5/3}$, where k is the wavenumber. The recent study by Manucharyan & Thompson (2022) on ice-covered regions suggests that these slopes may differ from the conventional values observed in the open ocean. Within the ML, spectral slopes of shallower than $\sim k^{-5/3}$, associated with an inverse energy cascade, are prominent in our simulations during winter for most of the wavenumbers, including the mesoscale and submesoscale ranges. Meanwhile, slopes of k^{-3}, corresponding to a forward energy cascade, occur in summer for scales smaller than the R_D, i.e. over the submesoscale range.

Power laws are a good indication of the inverse and forward energy cascades (Vallis, 2017), but a more quantitative estimate of the seasonal variability of the energy cascades is performed by computing the KE fluxes (Eq. 5). The seasonally averaged spectral fluxes correspond to the energy transfer to transition from the energy distribution from the snapshot of the spectra at the beginning of a given season to the snapshot of the spectra at the beginning of the following season. Positive values of the KE flux indicate a forward energy cascade (energy is transferred from large to small scales), while negative values correspond to the inverse energy cascade (energy is transferred from small to large scales). During summer (JJA), the KE flux (Fig. 6c) shows a pronounced inverse cascade at scales larger than $5km$ and a weak forward energy at smaller scales ($< 5km$). This indicates an important transfer of energy from submesoscale to mesoscale as the sea ice cover melts. Even after the ice has completely melted in autumn (SON), an inverse energy cascade persists, though reduced in magnitude and for larger lengthscales. In winter and spring there is both inverse and forward cascades contributing to upscaling energy to scales of $\sim 5km$ and dissipating energy, respectively. While there is still an inverse energy cascade during winter, its magnitude is lower than in summer. Note the shift of the KE flux minima towards larger wave numbers between winter and summer suggesting that the inverse energy cascade moves toward larger scales of motion between winter and summer. The ocean interior (150m depth) KE fluxes are one order of magnitude weaker (Fig. 6d), characterized by a forward cascade in summer and an inverse energy cascade during summer and autumn at scales comparable to the domain size ($\sim 100km$). Overall, the quantification of the energy fluxes showcase that the seasonality of the inverse energy cascade is constrained mostly to the ML and is responsible of the development and persistence of a mesoscale eddy field during summer.

3.3 Sources and sinks of kinetic energy

The seasonality of sea ice, along with the associated fluctuations in ML salinity due to the sea ice growth and melt, acts as a source and sink of potential energy, which can be converted into KE through the buoyancy flux. In particular, the baroclinic energy conversion (estimated from Eq. 2; Fig. 7a) plays a crucial role in energizing the mesoscale and submesoscale eddy field, since it is the pathway to transfer EPE into EKE. This conversion is more pronounced during winter and spring, coinciding with the largest addition of available potential energy to the ML, due to brine rejection during sea ice formation. In contrast, during the summer months, there is much less conversion from EPE to EKE due to the stable stratification of the water column when sea ice melts, leading to a weaker source of KE. In fact, in summer and autumn there are two maxima in the conversion term associated with the two peaks of stratification, one associated to the ML and and another one near the permanent halocline (Fig. 3c). Thus, the intensification of the mesoscale field in summer results from the inverse energy cascade of submesoscale features generated during the previous winter season, rather than a direct generation through baroclinic instability.

The baroclinic energy conversion shows a winter enhancement of baroclinic instabilities and a decrease in summer. To better understand the seasonality of instabilities, we examine the Eady time scale, and balanced Richardson number from the ageostrophic baroclinic instability theory. Longer Eady time scale are found in summer ($> 8hrs$; Eq. 12; Fig. 7b). In winter and spring, instabilities grow quicker, consistent with the development of submesoscale variability due to ML instabilities. Overall, the linear theory suggest a rapid growth of submesoscale in winter and a slower growth in summer (Fox-Kemper et al., 2008). The balanced Richardson angle further confirms that instabilities are present in the simulation (Thomas et al., 2013). In particular, values lower than the time-mean criteria described in Eq. 10 of $\sim -70°$ correspond to the development of symmetrical instabilities. Figure 7c shows that symmetric instabilities are generated within the ML over the full year, except during the ice-free months when the water column is more stable. In winter, the EPE conversion to EKE ($w'b'$) maintains the generation and energizing of the ocean submesoscale through symmetric instabilities, allowing the submesoscale to persist underneath the sea ice cover.

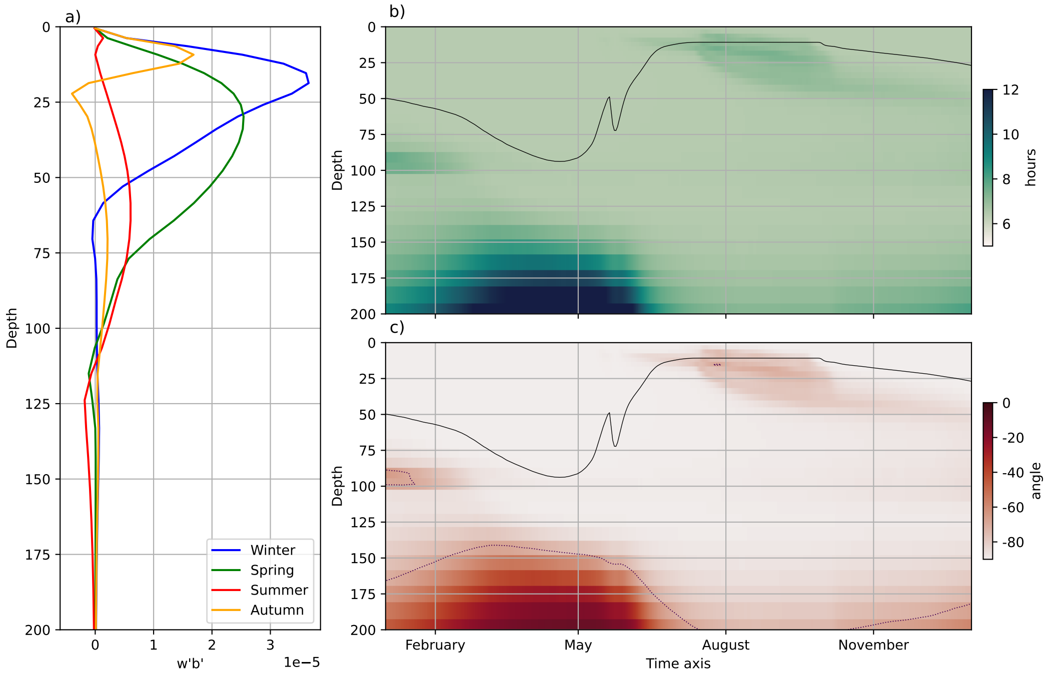

Figure 7. a) Profiles of the spatially averaged energy conversion term from EPE to EKE ($w'b'$; Eq. 2) for each season. Hovmöller diagrams of ageostrophic baroclinic instability properties such as b) the Eady time-scale (Eq. 12), and c) the balanced Richardson angle (Eq. 9). The solid lines and dotted line in panels b, and c show the ML depth and the mean stability criteria of the Richardson angle (Eq. 10), respectively

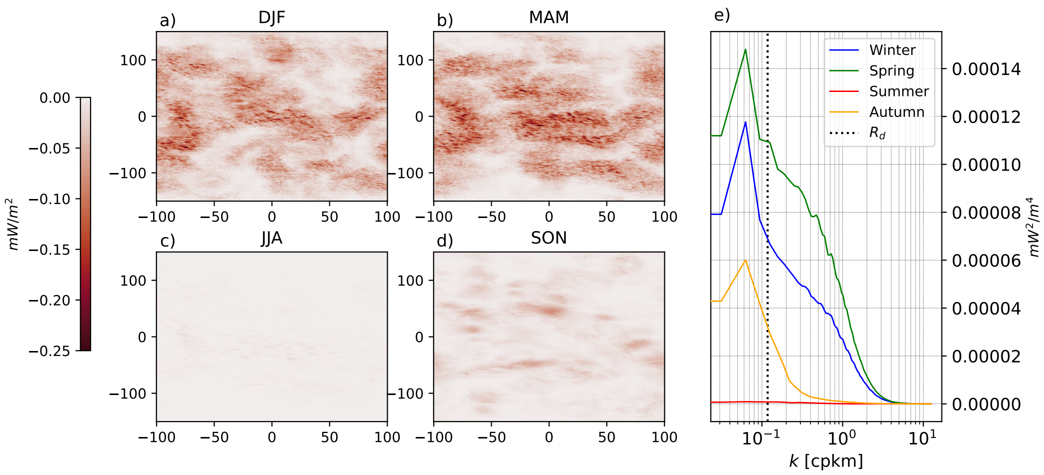

Figure 8. Spatial pattern of ice-induced eddy dissipation term (or ice work) for a) winter, b) spring, c) summer, and d) autumn. (e) Seasonal spectra of the ice-induced eddy dissipation term.

A sink of energy in the ML of our simulation is the dissipation due to the presence of sea ice. Figure 8 shows the averaged seasonal ice-induced eddy dissipation term estimated from Eq. 16. In winter and spring, the ice-covered seasons, the domain averaged ice-induced eddy dissipation is the largest at rates of -0.03 mW/m^2 and -0.04mW/m^2, respectively. As regions of the domain transition from ice-covered to ice-free and the ice concentration decreases from $\sim$ 100% to 0%, the ice-induced eddy dissipation in ice covered regions becomes almost negligible at -0.001 mW/m^2, since the ocean velocities and ice velocities are similar (Fig. 4b). Once the ice starts to grow again in September, the magnitude of the ice-induced eddy dissipation increases to -0.01 mW/m^2. Furthermore, the spectra of these fields show the dominant scale in which the ice-induced eddy dissipation acts (Fig. 8e). The spectra peak at scales of approximately 15 km, within the mesoscale range all year around, being the largest in winter and spring. At smaller scales than mesoscale, the spectra decrease in magnitude. Thus, the ice-induced eddy dissipation strongly dissipate mesoscale, while the submesoscale experiences a weaker ice-induced dissipation.

4 Conclusions

The pronounced seasonality of the ocean scales of motion and KE of seasonally ice-free oceans is largely driven by the interplay between eddies and sea ice. During summer, the absence of sea ice allows for the transfer of energy from smaller-scales (submesoscale) to larger scales (mesoscale) through an inverse energy cascade, resulting in the development and persistence of mesoscale eddies in summer. In winter, submesoscale is generated by symmetric instabilities and sea ice induces eddy dissipation (analogous to eddy-killing), where the mesoscale is preferentially dissipated by the ice work. Note that when the ice is mobile (i.e. at low ice concentrations), the ocean and ice scales of motion become similar and thus the stress is negligible. Meanwhile, when the ice is compact (high ice concentration), the ocean and ice scales of motion are different, and thus the stresses are larger. Thus, the seasonality of the inverse energy cascade and ice stress leads to a more active mesoscale field in summer and a weaker one in winter, while the submesoscale field is stronger in winter and weaker in summer. Therefore, in the seasonally ice-covered regions, the dynamical interactions between the ice and ocean can modulate the seasonality of the ocean scales and KE. Yet, it remains to include the interactions with the atmosphere (i.e. including winds) that can modify the sources and sinks of energy of the sea ice and the ocean.

Our results are consistent with previous studies suggesting that the regions of high ice concentration lack a seasonal cycle of the energy at mesoscale (Mensa & Timmermans, 2017), while regions with varying ice concentrations have a pronounced seasonality of the most energetic scales (Manucharyan & Thompson, 2022; Liu et al., 2024). This is likely consistent with observational evidence (Cassianides et al., 2023), but more observational data is required to corroborate it. Notably, the seasonality of scales and kinetic energy under ice cover differs from the seasonality of ice-free oceans, where only mesoscale is present in summer and mesoscale and submesoscale are both present in winter (Callies et al., 2015).

Here we use an elasto-visco-plastic rheology, but we hypothesize that using a different rheology or even a discrete floe-resolving sea ice models will likely reproduce the same ocean scale seasonality. This is because the key processes, such as the seasonality of the inverse energy cascade and ice-induced eddy dissipation, are inherent to the coupled interactions between the ice and ocean. However, our idealized setup ignores the effect of winds, which should be explored further to better understand how wind forcing impacts the seasonality of scales and KE in the ocean. In the presence of wind forcing, the coupling between the ocean, ice, and atmosphere may also modulate the seasonality of the scales, as wind stress would modify the ice-induced eddy dissipation.

These processes could have significant implications for the future of the Arctic Ocean. As the Arctic warms and sea ice continues to diminish, particularly during the summer, the Arctic eddy field is expected to become more energetic (Kim et al., 2023; Li et al., 2024). As the Arctic transitions to an ice-free summer, the seasonality of the inverse energy cascade, along with changes in the buoyancy fluxes, will modulate the persistence and energetics of the mesoscale field during the summer months. Additionally, the winter sea ice concentration and thickness have also decreased over the last few decades and are expected to continue to decline in the future (Wang et al., 2019), thus the ice-induced eddy dissipation may further weaken in the future, potentially altering the established seasonal energy cycle of the scales of motion in the Arctic. Therefore, understanding of the seasonality of the Arctic ocean KE is crucial for predicting the Arctic Ocean's energy distribution and variability, and its evolution in response to the ongoing changing climate.

5 Open Research

The idealized model configuration of the model are described and publicly available via (Martínez-Moreno, 2024a). All analyses and figures in this manuscript are reproducible via Jupyter notebooks and instructions can be found in the Zenodo archive `Ice-Ocean KE seasonality` via (Martínez-Moreno, 2024b).

Acknowledgments

We acknowledge funding from the ANR ImMEDIAT project (ANR-18-CE01-0010) and the MEDLEY project funded by the program JPI Ocean/JPI Climate (ANR-19-JPOC-0001) project. The idealized simulations and their analysis were performed using the HPC facilities DATARMOR of 'Pôle de Calcul Intensif pour la Mer' at Ifremer, Brest, France.

References

Bebieva, Y., & Timmermans, M.-L. (2016). An examination of double-diffusive processes in a mesoscale eddy in the Arctic Ocean. *Journal of Geophysical Research: Oceans*, *121*(1), 457-475. doi: https://doi.org/10.1002/2015JC011105

Blanke, B., & Delécluse, P. (1993). Variability of the tropical Atlantic ocean simulated by a general circulation model with two different mixed-layer physics. *Journal of Physical Oceanography*, *23*, 1363–1388. doi: 10.1175/1520-0485(1993)023⟨1363:VOTTAO⟩2.0.CO;2

Buckingham, C. E., Naveira Garabato, A. C., Thompson, A. F., Brannigan, L., Lazar, A., Marshall, D. P., ... Belcher, S. E. (2016). Seasonality of submesoscale flows in the ocean surface boundary layer. *Geophysical Research Letters*, *43*(5), 2118–2126.

Callies, J., Ferrari, R., Klymak, J. M., & Gula, J. (2015). Seasonality in submesoscale turbulence. *Nature communications*, *6*(1), 6862.

Capet, X., McWilliams, J. C., Molemaker, M. J., & Shchepetkin, A. F. (2008). Mesoscale to submesoscale transition in the California Current System. Part III: energy balance and flux. *Journal of Physical Oceanography*, *38*(10), 2256–2269.

Cassianides, A., Lique, C., Tréguier, A., Meneghello, G., & Marez, C. (2023). Observed spatio-temporal variability of the eddy-sea ice interactions in the Arctic Basin. *Journal of Geophysical Research: Oceans*, *128*(6). doi: 10.1029/2022jc019469

Charney, J. G. (1971). Geostrophic turbulence. *Journal of Atmospheric Sciences*, *28*(6), 1087 - 1095. doi: 10.1175/1520-0469(1971)028⟨1087:GT⟩2.0.CO;2

Cole, S. T., & Roemer, P. A. (2024). The transition layer and remnant transition layer of the Western Arctic Ocean: stratification, vertical diffusivity, and Pacific summer water heat fluxes. *Journal of Geophysical Research: Oceans*, *129*(2), e2023JC020059. (e2023JC020059 2023JC020059) doi: https://doi.org/10.1029/2023JC020059

Cole, S. T., Rudnick, D. L., & Colosi, J. A. (2010). Seasonal evolution of upper-

ocean horizontal structure and the remnant mixed layer. *Journal of Geophysical Research: Oceans*, *115*(C4).
Eady, E. T. (1949). Long waves and cyclone waves. *Tellus*, *1*(3), 33–52.
Ferrari, R., & Wunsch, C. (2009). Ocean circulation kinetic energy: reservoirs, sources, and sinks [Journal Article]. *Annual Review of Fluid Mechanics*, *41*(Volume 41, 2009), 253-282. doi: 10.1146/annurev.fluid.40.111406.102139
Fine, E. C., MacKinnon, J. A., Alford, M. H., & Mickett, J. B. (2018). Microstructure observations of turbulent heat fluxes in a warm-core Canada Basin eddy microstructure observations of turbulent heat fluxes in a warm-core Canada Basin eddy. *Journal of Physical Oceanography*, *48*(10), 2397–2418. doi: 10.1175/jpo-d-18-0028.1
Fofonoff, N. P., & Millard Jr, R. (1983). *Algorithms for the computation of fundamental properties of seawater*. UNESCO.
Fox-Kemper, B., Ferrari, R., & Hallberg, R. (2008). Parameterization of mixed layer eddies. Part I: theory and diagnosis. *Journal of Physical Oceanography*, *38*(6), 1145 - 1165. doi: 10.1175/2007JPO3792.1
Kim, Y.-H., Min, S.-K., Gillett, N. P., Notz, D., & Malinina, E. (2023). Observationally-constrained projections of an ice-free Arctic even under a low emission scenario. *Nature Communications*, *14*(1), 3139.
Large, W., & Yeager, S. (2009). The global climatology of an interannually varying air–sea flux data set. *Climate dynamics*, *33*, 341–364.
Li, X., Wang, Q., Danilov, S., Koldunov, N., Liu, C., Müller, V., … Jung, T. (2024). Eddy activity in the Arctic Ocean projected to surge in a warming world. *Nature Climate Change*, *14*(2), 156–162.
Lique, C., & Johnson, H. L. (2015). Is there any imprint of the wind variability on the Atlantic Water circulation within the Arctic Basin? *Geophysical Research Letters*, *42*(22), 9880-9888. doi: https://doi.org/10.1002/2015GL066141
Liu, C., Wang, Q., Danilov, S., Koldunov, N., Müller, V., Li, X., … Zhang, S. (2024). Spatial scales of kinetic energy in the Arctic Ocean. *Journal of Geophysical Research: Oceans*, *129*(3), e2023JC020013. (e2023JC020013 2023JC020013) doi: https://doi.org/10.1029/2023JC020013
Madec, G., Bourdallé-Badie, R., Chanut, J., Clementi, E., Coward, A., Ethé, C., … Moulin, A. (2022, March). *Nemo ocean engine.* Zenodo. doi: 10.5281/zenodo.6334656
Manucharyan, G. E., & Thompson, A. F. (2022). Heavy footprints of upper-ocean eddies on weakened Arctic sea ice in marginal ice zones. *Nature communications*, *13*(1), 2147.
Martínez-Moreno, J. (2024a). *josuemtzmo/Ocean_Ice_canal_HR_config: HR channel configuration of NEMO and SI3.* Zenodo. doi: 10.5281/zenodo.14204425
Martínez-Moreno, J. (2024b). *josuemtzmo/Seasonality_KE_under_ice: scripts, notebooks, and manuscript.* Zenodo. doi: 10.5281/zenodo.14204489
Meneghello, G., Marshall, J., Lique, C., Isachsen, P. E., Doddridge, E., Campin, J.-M., … Talandier, C. (2021). Genesis and decay of mesoscale baroclinic eddies in the seasonally ice-covered interior arctic ocean. *Journal of Physical Oceanography*, *51*(1), 115 - 129. doi: 10.1175/JPO-D-20-0054.1
Mensa, J. A., & Timmermans, M.-L. (2017). Characterizing the seasonal cycle of upper-ocean flows under multi-year sea ice. *Ocean Modelling*, *113*, 115–130. doi: 10.1016/j.ocemod.2017.03.009
NEMO Sea Ice Working Group. (2022, March). *Sea ice modelling integrated initiative (SI^3) – The NEMO sea ice engine* (No. 31). Zenodo. doi: 10.5281/zenodo.1471689
Nurser, A. J. G., & Bacon, S. (2014). The Rossby radius in the Arctic Ocean. *Ocean Science*, *10*(6), 967–975. doi: 10.5194/os-10-967-2014
Ou, H. W., & Gordon, A. L. (1986). Spin-down of baroclinic eddies under

sea ice. *Journal of Geophysical Research: Oceans*, *91*(C6), 7623-7630. doi: https://doi.org/10.1029/JC091iC06p07623

Pnyushkov, A., Polyakov, I. V., Padman, L., & Nguyen, A. T. (2018). Structure and dynamics of mesoscale eddies over the Laptev Sea continental slope in the Arctic Ocean. *Ocean science*, *14*(5), 1329–1347.

Qiu, B., Chen, S., Klein, P., Sasaki, H., & Sasai, Y. (2014). Seasonal mesoscale and submesoscale eddy variability along the North Pacific Subtropical Countercurrent. *Journal of Physical Oceanography*, *44*(12), 3079–3098.

Rai, S., Hecht, M., Maltrud, M., & Aluie, H. (2021). Scale of oceanic eddy killing by wind from global satellite observations. *Science Advances*, *7*(28), eabf4920. doi: 10.1126/sciadv.abf4920

Renault, L., Molemaker, M. J., Gula, J., Masson, S., & McWilliams, J. C. (2016). Control and stabilization of the gulf stream by oceanic current interaction with the atmosphere. *Journal of Physical Oceanography*, *46*(11), 3439 - 3453. doi: 10.1175/JPO-D-16-0115.1

Renault, L., Molemaker, M. J., McWilliams, J. C., Shchepetkin, A. F., Lemarié, F., Chelton, D., . . . Hall, A. (2016). Modulation of wind work by oceanic current interaction with the atmosphere. *Journal of Physical Oceanography*, *46*(6), 1685–1704.

Rocha, C. B., Gille, S. T., Chereskin, T. K., & Menemenlis, D. (2016). Seasonality of submesoscale dynamics in the Kuroshio Extension. *Geophysical Research Letters*, *43*(21), 11–304.

Stone, P. H. (1972). On non-geostrophic baroclinic stability: part III. The momentum and heat transports. *Journal of the Atmospheric Sciences*, *29*(3), 419–426.

Thomas, L. N., Taylor, J. R., Ferrari, R., & Joyce, T. M. (2013). Symmetric instability in the Gulf Stream. *Deep Sea Research Part II: Topical Studies in Oceanography*, *91*, 96–110.

Timmermans, M.-L., Cole, S., & Toole, J. (2012). Horizontal density structure and restratification of the Arctic Ocean surface layer. *Journal of Physical Oceanography*, *42*(4), 659 - 668. doi: 10.1175/JPO-D-11-0125.1

Uchida, T., Abernathey, R., & Smith, S. (2017). Seasonality of eddy kinetic energy in an eddy permitting global climate model. *Ocean Modelling*, *118*, 41-58. doi: https://doi.org/10.1016/j.ocemod.2017.08.006

Vallis, G. K. (2017). *Atmospheric and oceanic fluid dynamics.* Cambridge University Press.

Wang, Y., Bi, H., Huang, H., Liu, Y., Liu, Y., Liang, X., . . . Zhang, Z. (2019). Satellite-observed trends in the Arctic sea ice concentration for the period 1979–2016. *Journal of Oceanology and Limnology*, *37*(1), 18–37.

Watanabe, E., Onodera, J., Harada, N., Honda, M. C., Kimoto, K., Kikuchi, T., . . . others (2014). Enhanced role of eddies in the Arctic marine biological pump. *Nature Communications*, *5*(1), 3950.

Wunsch, C., & Ferrari, R. (2004). Vertical mixing, energy, and the general circulation of the oceans. *Annu. Rev. Fluid Mech.*, *36*(1), 281–314.

Yu, Y., Sandwell, D., & Gille, S. (2023). Seasonality of the sub-mesoscale to mesoscale sea surface variability from multi-year satellite altimetry. *Journal of Geophysical Research: Oceans*, *128*(2), e2022JC019486.

Zhai, L., & Li, T. (2023). Seasonal variability of the mixed layer depth determined using an improved maximum angle method in the Arctic Basins. *Journal of Oceanology and Limnology*, *41*(3), 852–864.

Zhao, M., Timmermans, M.-L., Cole, S., Krishfield, R., Proshutinsky, A., & Toole, J. (2014). Characterizing the eddy field in the Arctic Ocean halocline. *Journal of Geophysical Research: Oceans*, *119*(12), 8800–8817.